16TH EUROPEAN CONFERENCE ON EARTHQUAKE ENGINEERING THESSALONIKI 18 - 21 JUNE 2018

FIBRE-BASED CAPACITY MODEL FOR URM PIERS SUBJECTED TO COMBINED IN-PLANE AND OUT-OF-PLANE ACTIONS

Fulvio PARISI[1], Elia ACCONCIA[2]

ABSTRACT

Seismic performance of masonry buildings is usually assessed at local and global levels, separately. Seismic safety against local collapse mechanisms is evaluated via macroblock models and linear/nonlinear kinematic analysis methods. Conversely, safety against in-plane failure modes is assessed through nonlinear static/dynamic analysis of global macroelement models. Nonetheless, the in-plane seismic capacity of masonry walls can be strongly influenced by simultaneous response to out-of-plane actions. Although this issue has been recently investigated in a few experimental programs and numerical studies, the level of knowledge is still limited.
In this study, the authors present a novel fiber-based capacity model that allows performance-based seismic design/assessment of unreinforced masonry piers subjected to combined in-plane and out-of-plane loading. Based on a nonlinear incremental analysis procedure, moment–curvature diagrams are derived at different levels of axial load and 3D flexural strength domains are developed at five performance limit states. Nonlinear sectional capacity under biaxial bending and axial loading is directly governed by the macroscopic constitutive model assigned to masonry and sectional shape. Analysis results show a strong interaction between bending moments related to in-plane and out-of-plane loading, which changes with the axial load level. Simplified biaxial interaction models are derived through nonlinear regression analysis for engineering practice. It is shown that the axial load level and ratio between in-plane and out-of-plane actions has an impact on sectional ductility at different limit states. The capacity model allows considering the softened response of masonry sections under increasing axial load levels, which also induces a reduction in ultimate axial load.

Keywords: Masonry walls; Combined in-plane and out-of-plane loading; Analytical capacity model; Performance limit states; Biaxial bending–axial load interaction models

1. INTRODUCTION

Nonlinear behavior of masonry walls under in-plane (IP) and out-of-plane (OOP) actions has been usually investigated through different capacity models and analysis methods. Nevertheless, destructive earthquakes have shown that nonlinear response of masonry buildings can be affected by the interaction between in-plane and out-of-plane damage (e.g. Parisi and Augenti 2013a). Some recent experimental campaigns and numerical investigations have further confirmed a strong IP-OOP interaction. Najafgholipour et al. (2013) conducted a series of tests on brick masonry panels subjected in-plane shear loading and out-of-plane bending. Both the experimental results and the numerical model calibrated by those researchers have highlighted that the longitudinal slenderness of walls strongly influences the interaction level. The latter was characterized up to the peak strength. Three slenderness levels were investigated and as many interaction curves were obtained. It was thus obtained an interaction model that provides the minimum envelope of the abovementioned three curves.
Agnihotri et al. (2013) further investigated the IP-OOP interaction from a numerical point of view. A nonlinear finite element (FE) model of unreinforced masonry (URM) walls with different levels of longitudinal and transverse slenderness was developed. The interaction was evaluated by considering

[1]Assistant Professor, University of Naples Federico II, Naples, Italy, fulvio.parisi@unina.it
[2]Research fellow, University of Naples Federico II, Naples, Italy, elia@studioacconcia.it

cyclic in-plane drifts and monotonically increasing out-of-plane pressures. It was then assessed the out-of-plane capacity reduction due to the in-plane damage of the wall.
Najafgholipour et al. (2014) carried out a numerical sensitivity study based on an anisotropic macromodel, demonstrating that the IP-OOP interaction depends not only on the longitudinal slenderness of the wall but also on the elastic and inelastic properties of the masonry in tension. Based on numerical results, an empirical capacity model was obtained for predicting the resistance in one direction from the load in the orthogonal direction.
Dolatshahi et al. (2015) applied the macromodeling technique to different masonry panels, obtaining IP-OOP interaction curves and comparing results with those derived from FE analysis.
Due to the importance of the problem, the authors of this paper extended a theoretical research program that initially focused on assessing the strength and deformation capacities of URM cross sections subjected to uniaxial bending and axial load (Parisi and Augenti 2013b, Parisi et al. 2016). This mechanical behavior has been investigated considering a wide variety of macroscopic constitutive models available in literature for ordinary masonry. Parisi and Augenti (2013b) quantified the influence of the strength degradation of masonry on bending moment–axial load interaction domains, considering their variation with strain ductility that was taken as third dimension of the sectional capacity model. More recently, Parisi et al. (2016) identified the constitutive models that provide the best estimate of the moment–curvature behavior of rectangular URM cross sections made of clay brick masonry, calcarenite stone masonry or one of them without distinction. Therefore, the aim of this paper is to evaluate the effects of IP-OOP interaction along the principal axes of rectangular cross sections, both in terms of strength and deformation capacity.

2. METHODOLOGY

This analytical study focuses on the flexural response of URM walls to in-plane and out-of-plane point lateral loads that statically simulate the inertia forces transmitted by floor diaphragms in buildings. Particularly in the case of existing URM buildings not designed for earthquake resistance, the magnitude of out-of-plane seismic actions distributed by flexible floors (made of, for instance, timber/steel joist systems without rigid slab) can be significantly higher than that of inertia pressures associated with the selfweight of walls. This means that distributed out-of-plane pressures as those considered in previous studies (e.g. Agnihotri et al. 2013) were replaced by lateral forces acting on top of the wall. Assuming nonlinear constitutive models of URM assemblages selected by Parisi et al. (2016) and that plane sections remain plane after flexural deformation, this study consisted of the steps described below.

1. Derivation of moment–curvature diagrams corresponding to each selected constitutive model, given the axial load on the section. Each diagram was obtained by changing the angle ϑ between the resulting moment vector $\mathbf{M} = [M_x, M_y]$ and the x-axis of the section.
2. Definition of five limit states in terms of tensile/compressive strength limit at material level or resisting bending moment at sectional level.
3. Identification of the limit states on each moment–curvature diagram and deriving the corresponding N–M_x–M_y three-dimensional (3D) interaction domains.
4. Derivation of M_x–M_y two-dimensional (2D) interaction domains by sectioning 3D domains at prescribed levels of axial load.
5. Regression analysis of M_x–M_y data corresponding to each group of constitutive models and derivation of a simplified capacity model that allows predicting the peak resisting moment in a principal direction of cross section given the axial load and bending moment in the perpendicular direction.

The URM cross section was assumed to have length L and thickness T. The cross section was discretized in 900 fibers, which is an optimal number evaluated through a sensitivity analysis. For all the selected constitutive models, the tensile behavior of masonry was assumed to be characterized by a linear elastic branch up to peak tensile strength and a linear softening branch until the ultimate tensile strain is reached. The Young's moduli in tension and compression were assumed to be the same.

3. NONLINEAR MOMENT–CURVATURE ANALYSIS

3.1 Computational procedure

An iterative incremental procedure of sectional analysis was developed in MATLAB® to perform numerical integration of constitutive equations or stress–strain data sets. Given the axial load and a couple of in-plane and out-of-plane lateral loads on the URM wall (i.e. F_{ip} and F_{oop} in Figure 1), the relationship between bending moments M_x and M_y of the most stressed section is known. In the nonlinear analysis procedure, the authors parameterized the ratio M_x/M_y through the biaxial bending angle
$\vartheta = \tan^{-1}(M_y/M_x)$. The distributions of stresses and strains over the cross section were obtained by assuming two parameters, i.e. bending curvature φ and ϑ, as well as the axial load (Figure 2). The curvature components φ_x and φ_y along the x-axis and y-axis of cross section were defined as follows:

$$\varphi_x = -\frac{\varphi}{\sqrt{1+\tan^2\vartheta}} \tag{1}$$

$$\varphi_y = \frac{\varphi\tan\vartheta}{\sqrt{1+\tan^2\vartheta}} \tag{2}$$

Both mechanical and geometrical nonlinearities are taken into account, the latter being related to the fact that the effective cross section depends on the relative magnitude of lateral loads.

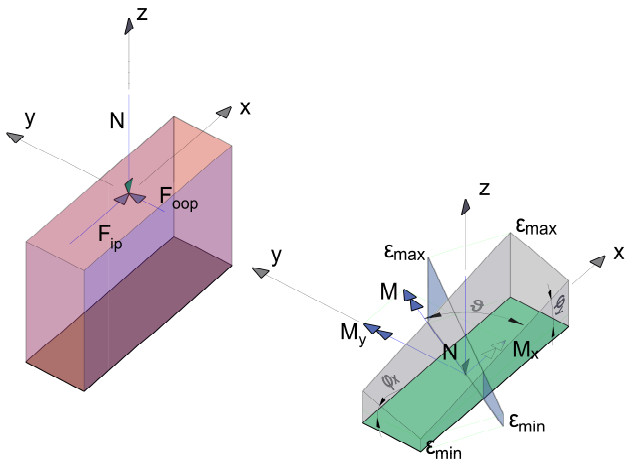

Figure 1. Masonry wall subjected to in-plane and out-of-plane loading

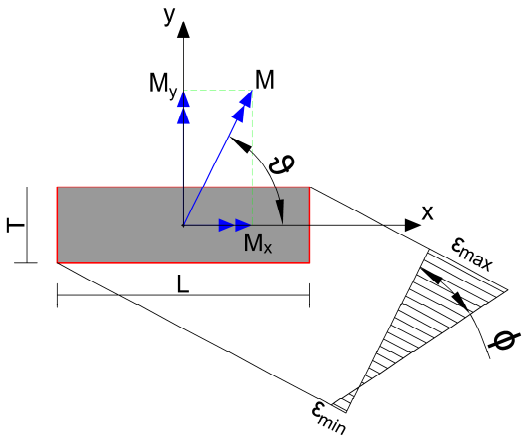

Figure 2. Relationship between moment vector **M**, biaxial bending angle ϑ and curvature φ

Figure 3 shows a flowchart in which the incremental iterative analysis is summarized.

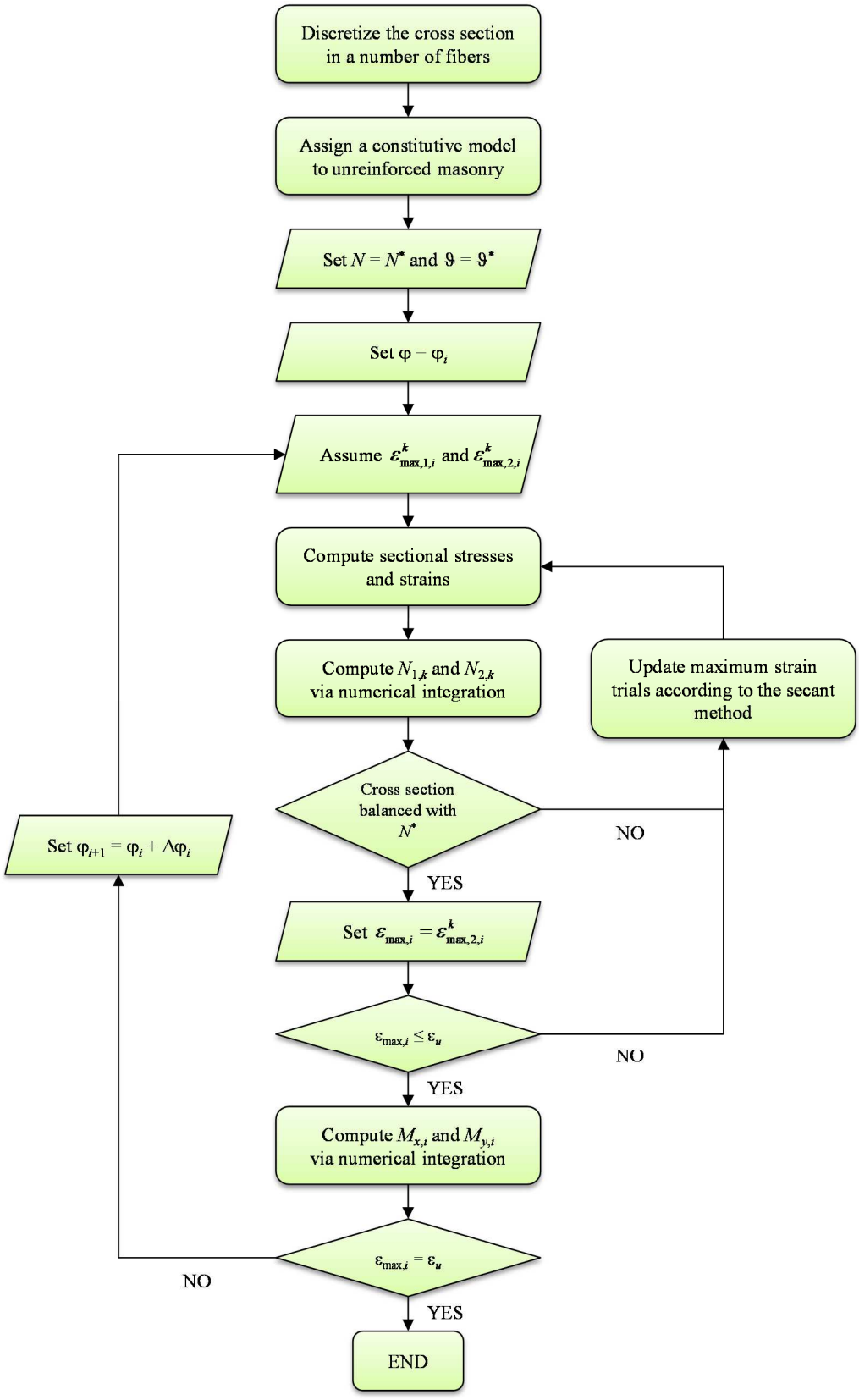

Figure 3. Flowchart of the incremental iterative procedure

The moment–curvature diagram of the URM cross section is derived through the following main steps where i and k denote the curvature increment and iteration within each increment, respectively:

1. Discretize the URM cross section into a number n of fibers with sectional area $A_f = LT/n$.
2. Assign a constitutive model (in the form of either stress–strain equations or data sets) to masonry in tension and compression.
3. Set the axial load level $N = N^*$ and biaxial bending angle $\vartheta = \vartheta^*$.
4. Set the bending curvature $\varphi = \varphi_i$.
5. Assume two trials of maximum axial strain $\varepsilon^k_{\max,1,i}$ and $\varepsilon^k_{\max,2,i}$ in order to search the actual value $\varepsilon_{\max}$ corresponding to the i-th level of bending curvature. $\varepsilon^k_{\max,1,i}$ is set equal to the maximum axial strain that would occur if the sectional behavior is linear, whereas the second strain trial is defined as $\varepsilon^k_{\max,2,i} = 0.5\varepsilon^k_{\max,2,i}$. The values assigned to $\varepsilon^k_{\max,1,i}$ and $\varepsilon^k_{\max,2,i}$ have significant influence on the convergence rate of the algorithm.
6. Compute the sectional distribution of axial strains $\varepsilon(x,y)^k_i$ corresponding to each maximum strain trial, given the assumption of plane section after flexural deformation.
7. Compute the sectional distribution of axial stresses $\sigma\left[\varepsilon(x,y)^k_i\right]$ corresponding to each maximum strain trial.
8. Calculate the axial loads $N_{1,k}$ and $N_{2,k}$ through numerical integration of axial stresses corresponding to $\varepsilon^k_{\max,1,i}$ and $\varepsilon^k_{\max,2,i}$.
9. Check that the following inequality is met:

$$\left|\frac{N_{2,k} - N^*}{N^*}\right| < tol_N \tag{3}$$

   If inequality 3 is not satisfied, repeat steps 6–9 by changing $\varepsilon^k_{\max,1,i}$ and $\varepsilon^k_{\max,2,i}$ until convergence is reached. Otherwise, the distribution of axial strains corresponding to $\varepsilon^k_{\max,2,i}$ allows sectional balance with the given axial load.
10. Set the actual maximum strain $\varepsilon_{\max,i} = \varepsilon^k_{\max,2,i}$.
11. Check that the maximum axial strain does not exceed the ultimate strain of masonry in compression, that is:

$$\varepsilon_{\max,i} \le \varepsilon_u \tag{4}$$

12. If inequality 4 is not met, repeat steps 6–11 till convergence. Otherwise, compressive failure is not reached.
13. Compute the bending moments $M_{x,i}$ and $M_{y,i}$ through numerical integration of axial stresses.
14. Assume a curvature increment $\Delta\varphi_i > 0$, set $\varphi_{i+1} = \varphi_i + \Delta\varphi_i$ and repeat steps 5–13 until ultimate strain of masonry is achieved.

This incremental iterative procedure was implemented according to the secant method where numerical tolerance on axial load was assumed to be $tol_N = 10^{-7}$. In detail, the secant method was used when changing $\varepsilon^k_{\max,1,i}$ and $\varepsilon^k_{\max,2,i}$ in subsequent iterations.

3.2 Moment–curvature diagrams and limit states

The procedure described above allowed the moment–curvature diagrams to be obtained under varying angle ϑ and axial load N. Figure 4 shows dimensionless moment–curvature diagrams in which bending moment M is normalized to a geometric parameter H times the maximum axial load capacity N_m and the bending curvature φ is normalized to H. In case of biaxial bending, H was defined as a nonlinear transformation of M_x, M_y, L and T, according to moment vector decomposition along the principal axes of the cross section. Each moment–curvature diagram is associated with a given axial

load normalized to the maximum axial load capacity, i.e. N/N_m. Numerical integration was carried out by assuming the constitutive model proposed by Augenti and Parisi (2010) for masonry subjected to compression perpendicular to bed joints. Moment–curvature diagrams were derived for three values of biaxial bending angle, i.e. 0, π/8 and π/4.

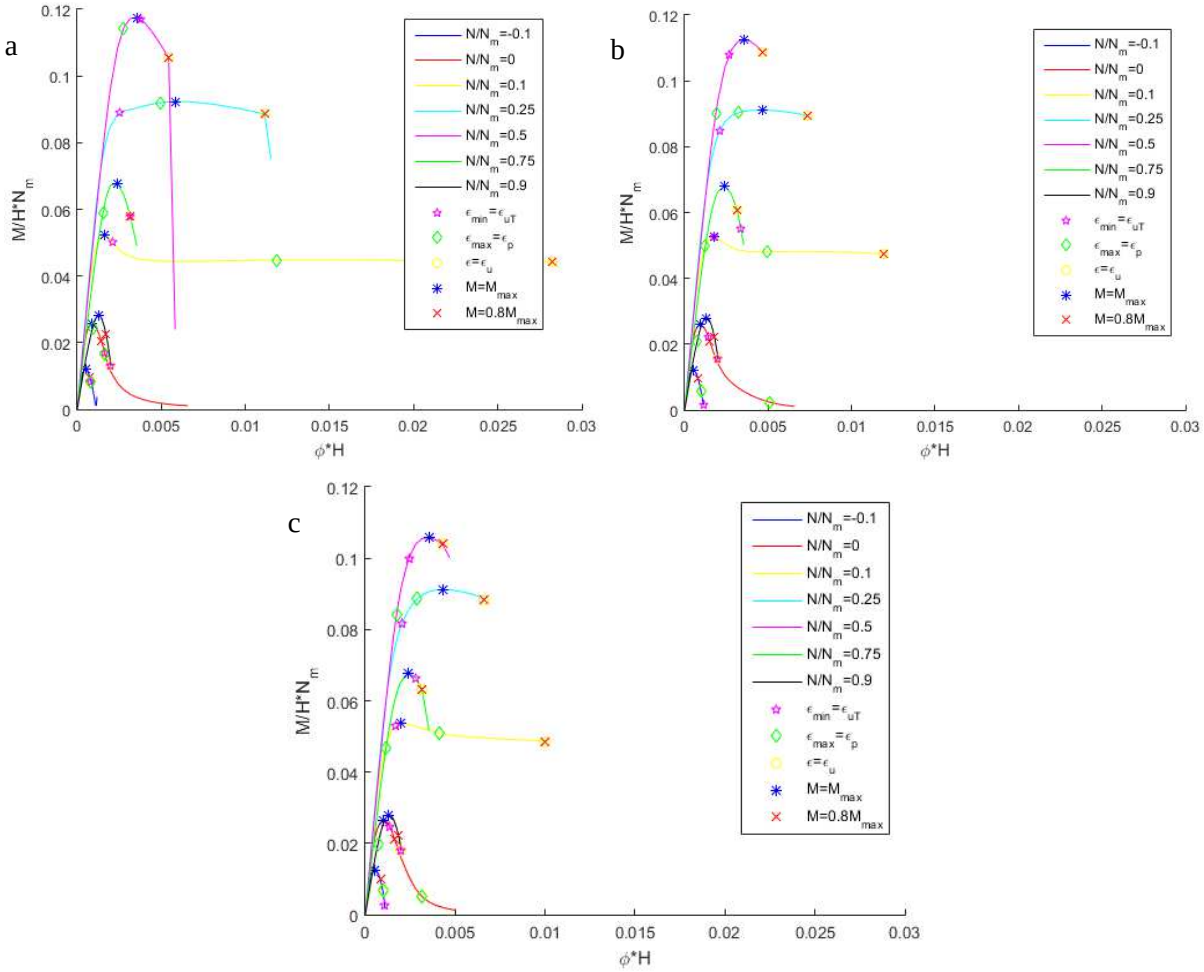

Figure 4. Moment–curvature diagrams and sectional limit states corresponding to different angles of biaxial bending: (a) ϑ = 0; (b) ϑ = π/8; (c) ϑ = π/4

The following limit states were considered and identified on moment–curvature diagrams:

- Minimum axial strain that reaches the ultimate tensile strain of masonry (i.e. $\varepsilon_{min} = \varepsilon_{uT}$).
- Maximum axial strain that reaches the limit elastic strain of masonry in compression (i.e. $\varepsilon_{max} = \varepsilon_p$), which was associated with the peak compressive strength.
- Maximum axial strain that reaches the ultimate compressive strain of masonry (i.e. $\varepsilon_{max} = \varepsilon_u$).
- Resisting moment that reaches the maximum value $M = M_{max}$.
- Resisting moment that reaches a 20% degradation on the post-peak softening branch of the moment–curvature diagram (i.e. $M = 0.8M_{max}$).

Therefore, three limit states capture the attainment of axial strain limits and the other two limit states identify the peak bending resistance and ultimate bending resistance that can be conventionally assumed in sectional design for the life safety limit state.

Analytical results highlight the following characteristics of nonlinear sectional behavior when URM is assumed to have a non-zero tensile strength and strain softening in compression:

- Non-zero bending capacity can be observed when the URM cross section is subjected biaxial bending with zero or negative axial loading (i.e. tension). In such conditions, the sectional behavior is mainly influenced by tensile masonry properties and ultimate compressive strain is far from being achieved.

- If biaxial bending is combined with compressive axial loading, the sequence of strain-based limit states (particularly the attainment of ultimate tensile strain and limit elastic compressive strain) can change with the magnitude of the normalized axial load.
- Softening plays a key role in the simulation of nonlinear sectional behavior, especially when $N/N_m \leq 0$ or $N/N_m \geq 0.5$.
- The magnitude of axial load has a significant impact on both sectional resistance and ultimate curvature, with the highest levels of bending moment and deformation capacity reached when $N/N_m = 0.5$ and $N/N_m = 0.1$, respectively. In the latter case of axial loading, the 20% degradation of bending resistance is reached simultaneously with the ultimate compressive strain of masonry or it may even not be attained.

As N/N_m increases from –0.1 to 0.9, the resisting bending moment first increases up to the maximum value at $N/N_m = 0.5$ and then decreases until the minimum resistance under compressive axial loading is reached. Nonetheless, the minimum level of peak resisting moment is attained when tensile axial loading is applied.

4. 3D INTERACTION DOMAINS

For each constitutive model selected in Parisi et al. (2016), each limit state and each axial load level, the authors computed the resisting moments and plotted a dimensionless 3D interaction domain that allows the IP-OOP interaction to be considered in safety verifications. Figures 4(a)–(e) show the five interaction domains corresponding to the previously considered constitutive model.

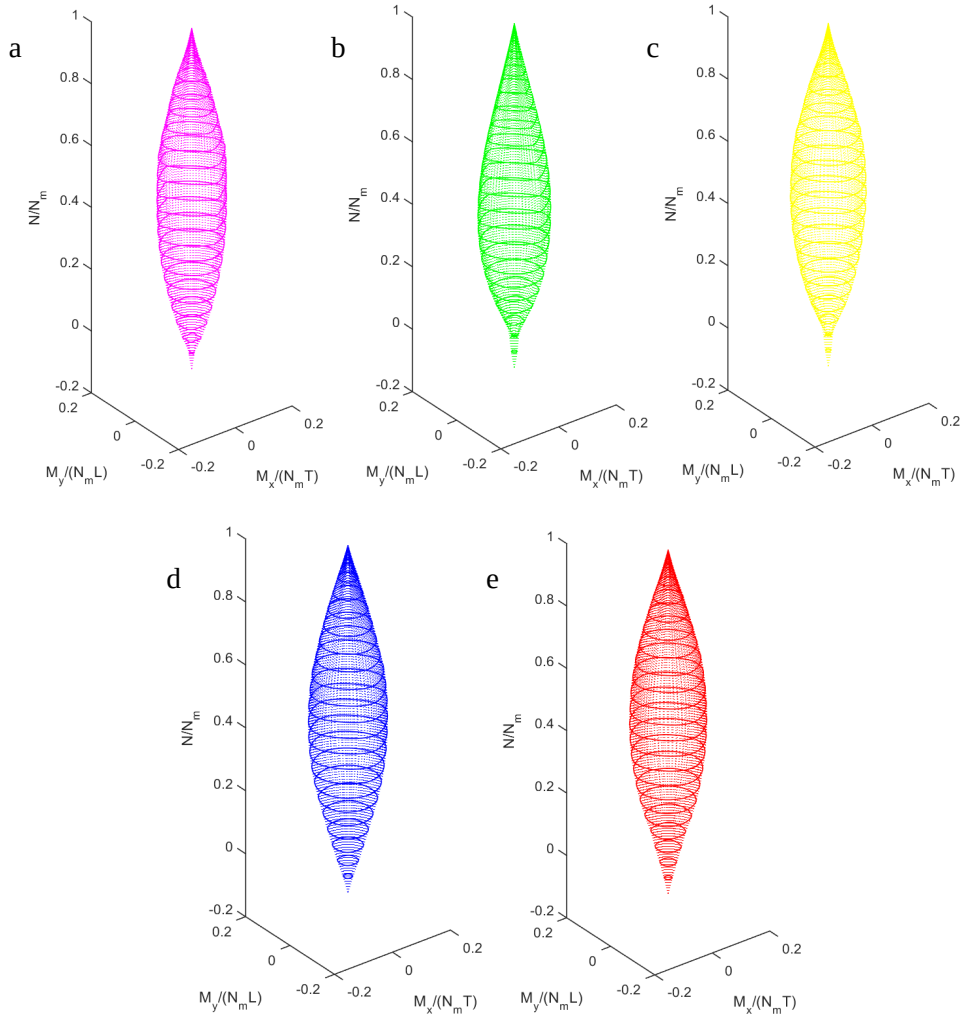

Figure 1. Dimensionless 3D interaction domains associated with following limit states: (a) $\varepsilon_{min} = \varepsilon_{uT}$; (b) $\varepsilon_{min} = \varepsilon_p$; (c) $\varepsilon_{min} = \varepsilon_u$; (d) $M = M_{max}$; (e) $M = 0.8M_{max}$

The interaction domains confirm that the URM cross section can have a non-zero bending resistance at low levels of tensile axial loading. In this respect and in the case of uniaxial bending, Parisi et al. (2016) demonstrated that tensile strength plays a role especially at high levels of axial load, influencing the bending stiffness and maximum bending strength. Such interaction domains can be useful in macroelement capacity models of URM buildings that include degrees of freedom associated with both in-plane and out-of-plane deformations of loadbearing walls.

5. SIMPLIFIED BIAXIAL INTERACTION MODEL

The selection of three different groups of constitutive models for masonry in compression resulted in a considerable amount of interaction domains and moment–curvature diagrams. If the nonlinear analysis procedure described in Sect. 3 is not computationally efficient, for instance because many simulations must be run on a whole building structure, the M_x–M_y interaction can be still considered through a simplified model derived through regression analysis of detailed results. In this study, the authors performed nonlinear regression on data sets corresponding to each selected group of constitutive models and each limit state considered. The following interaction model was selected:

$$\left(\frac{\bar{M}_x}{\bar{M}_{Rx}}\right)^{\alpha}+\left(\frac{\bar{M}_y}{\bar{M}_{Ry}}\right)^{\beta}=1 \tag{5}$$

where: $\bar{M}_x = M_x / N_m T$ and $\bar{M}_y = M_y / N_m L$ are the normalized bending moments having the vectors directed along the x- and y-axis of the cross section; $\bar{M}_{Rx} = M_{Rx} / N_m T$ and $\bar{M}_{Ry} = M_{Ry} / N_m L$ are the bending moment capacities evaluated in the case of uniaxial bending combined with axial loading, for the limit state under consideration; and α and β are regression coefficients. Based on the dimensionless format of 3D interaction domains, the authors assumed $\alpha = \beta$ and $M_{Rx} = M_{Ry} = M_R$, allowing Equation 5 to be specialized as follows:

$$\bar{M}_y = \left(\bar{M}_R^{\alpha} - \bar{M}_x^{\alpha}\right)^{\frac{1}{\alpha}} \tag{6}$$

Actually, α and β were also separately determined through regression analysis, but their values were found to be approximately the same. Regression analysis allowed the authors to develop a series of abacuses, each of them related to a prescribed limit state and one of the three groups of constitutive models. Dealing with the limit state of peak resistance (i.e. $M = M_{max}$), Table 1 provides the values of α and $\bar{M}_R$ that allows the mean dimensionless moment capacity $\bar{M}_y$ under biaxial bending to be computed through Equation 6.

Table 1. Parameters of simplified interaction model for the limit state $M = M_{max}$

N/N_m	α	$\bar{M}_R$	σ
–0.05	2.505	0.013	2.78E-04
0	2.374	0.028	7.10E-04
0.05	2.247	0.043	9.73E-04
0.1	2.132	0.056	1.09E-03
0.15	2.081	0.068	1.14E-03
0.2	2.120	0.080	9.98E-04
0.25	1.948	0.093	5.28E-04
0.3	1.842	0.104	6.57E-04
0.35	1.762	0.113	9.75E-04
0.4	1.707	0.119	1.60E-03
0.45	1.666	0.122	2.17E-03
0.5	1.636	0.122	2.73E-03

0.55	1.593	0.120	3.18E-03
0.6	1.611	0.114	4.16E-03
0.65	1.689	0.103	7.88E-03
0.7	1.861	0.087	6.68E-03
0.75	1.834	0.074	4.63E-03
0.8	2.238	0.058	4.20E-03
0.85	2.236	0.045	2.15E-03
0.9	2.220	0.031	1.85E-03

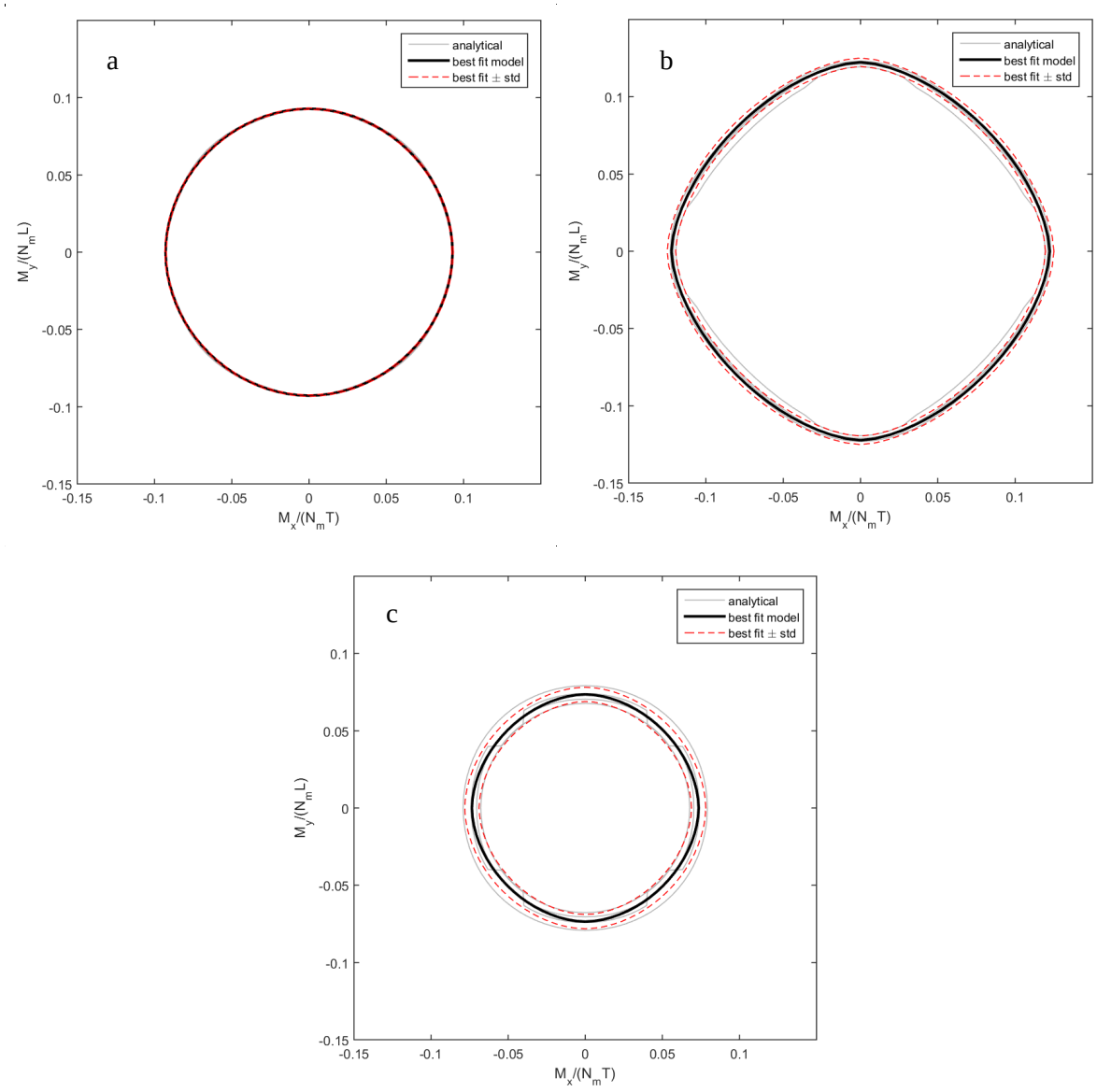

Figure 2. Simplified M_x–M_y interaction domains for the limit state $M = M_{max}$ and constitutive models of calcarenite masonry: (a) $N/N_m = 0.25$; (b) $N/N_m = 0.50$; (c) $N/N_m = 0.75$

Table 1 provides also the standard deviation of $\bar{M}_y$, denoted by σ, which quantifies the uncertainty in the M_x–M_y interaction model. In this regard, Figures 5(a), 5(b) and 5(c) show the dimensionless interaction curves corresponding to $N/N_m = 0.25$, $N/N_m = 0.5$ and $N/N_m = 0.75$, respectively, for the limit state of peak resistance and the group of constitutive models selected by Parisi et al. (2016) for calcarenite masonry.

When the magnitude of axial load is high, the uncertainty level of the regression model is rather high, as demonstrated by the larger bandwidth *best fit* ± *std* shown in Figure 5(c). The parameters $\bar{M}_R$ and α characterize the size and shape of the interaction domain. In detail, $\bar{M}_R$ is the abscissa at which $\bar{M}_y$ vanishes, so it defines the size of the interaction domain. The parameter α defines the shape of the domain. If $\alpha = 1$, the dimensionless interaction curve turns out to be squared and rotated of $\pi/4$, establishing a linear IP-OOP interaction. In that case, the bending moment M decreases as the angle ϑ increases from 0 to $\pi/4$ and then increases as ϑ further increases from $\pi/4$ to $\pi/2$. If $\alpha = 2$, the dimensionless interaction curve becomes a circle and M does not still depend on ϑ. If $\alpha > 2$, M increases as ϑ increases in the range $[0,\pi/4]$ and then decreases as ϑ increases in the range $[0,\pi/2]$. The regression analysis results in Table 1 show $\alpha > 2$ if N/N_m falls in the interval [–0.05,0.2] or [0.8,0.9]. By contrast, α decreases up to values approximately equal to 1.6 as N/N_m increases or decreases towards 0.5. The variation in M with ϑ indicates the influence of the simultaneous presence of M_x and M_y. If $\alpha < 2$, the higher intensity of the bending moment in one direction induces an increase in the resulting moment M, the opposite occurring in the presence of both bending moment components. If $\alpha > 2$, the simultaneous presence of M_x and M_y produces an increase in M. This was found to be a general outcome, regardless of the limit state under consideration.

6. CONCLUSIONS

A nonlinear analysis procedure based on fiber modeling of URM cross sections subjected to biaxial bending and axial loading was developed. Based on a previous selection of constitutive models, moment–curvature diagrams at different levels of normalized axial load were derived, identifying the attainment of five limit states defined in terms of axial strains or bending moment capacity. Detecting the considered limit states allowed 3D interaction domains to be plotted in a dimensionless format that removes dependency on section dimensions and masonry strength. Those interaction domains combined with moment–curvature diagrams allows a detailed flexural capacity modeling of URM cross sections in walls subjected to combined in-plane and out-of-plane lateral actions.

A large number of analytical N–M_x–M_y interaction domains corresponding to different sets of constitutive models were cut at several axial load levels. Regression analysis of analytical data sets allowed a simplified (empirical) M_x–M_y interaction model to be characterized at each N-level, providing a set of abacuses for each limit state and selected group of constitutive models. Both mean and dispersion in moment capacity estimation can be considered, allowing model uncertainty to be taken into account. Given the bending moment in one principal direction of the cross section, the simplified interaction model allows the bending moment capacity in the perpendicular direction to be estimated.

Both detailed and simplified capacity models include the effects of mechanical nonlinearity in tension and compression, as well as the impact of geometrical nonlinearity due to tensile cracking in both directions of the cross section. In cases of URM walls subjected to medium levels of axial load and/or characterized by low shear strength or low in-plane slenderness ratio, the IP-OOP interaction can be also influenced by shear deformation, resulting in a potential shear or mixed flexural-shear failure mode. In such cases, the flexural capacity model proposed in this study cannot be used alone so it should be extended or combined with other shear capacity models. This motivates further research on IP-OOP interaction through experimental, numerical and analytical approaches.

ACKNOWLEDGMENTS

This experimental research was carried out in the framework of the 2016-2017 ReLUIS-DPC research projects supported by the Italian Civil Protection Department.

REFERENCES

Agnihotri P, Singhal V, Rai DC (2013). Effect of in-plane damage on out-of-plane strength of unreinforced masonry walls. *Engineering Structures*, 57: 1-11.

Augenti N, Parisi F (2010). Constitutive models for tuff masonry under uniaxial compression. *Journal of Materials in Civil Engineering*, 22(11): 1102-1111.

Dolatshahi KM, Aref AJ, Whittaker AS (2015). Interaction curves for in-plane and out-of-plane behaviors of unreinforced masonry walls. *Journal of Earthquake Engineering*, 19(1): 60-84.

Najafgholipour MA, Maheri MR, Lourenço PB (2013). Capacity interaction in brick masonry under simultaneous in-plane and out-of-plane loads. *Construction and Building Materials*, 38: 619-626.

Najafgholipour MA, Maheri MR, Lourenço PB (2014). Definition of interaction curves for the in-plane and out-of-plane capacity in brick masonry walls. *Construction and Building Materials*, 55: 168-182.

Parisi F, Augenti N (2013a). Earthquake damages to cultural heritage constructions and simplified assessment of artworks. *Engineering Failure Analysis*, 34: 735-760.

Parisi F, Augenti N (2013b). Assessment of unreinforced masonry cross sections under eccentric compression accounting for strain softening. *Construction and Building Materials*, 41: 654-664.

Parisi F, Sabella G, Augenti N (2016). Constitutive model selection for URM cross sections based on best-fit analytical moment–curvature diagrams. *Engineering Structures*, 111: 451-466.